

# Efficient perfectly vertical fiber-to-chip grating coupler for silicon horizontal multiple slot waveguides

John Covey\* and Ray T. Chen

The University of Texas at Austin, 10100 Burnet Road Bldg. 160 MER, Austin, Texas 78758, USA  
\*john.covey@coveytech.com

**Abstract:** Horizontal multiple slot waveguides of polysilicon and silicon nanocrystalline oxide were grating coupled to a surface normal fiber array. Measurements yielded a coupling efficiency of 60% per grating. The fabrication-tolerant, four-stage grating design was genetically evolved from a random seed without starting from first-principle design. Theoretical coupling efficiency was 68% and was re-designed to 63% after accommodating all sources of fabrication error. To our knowledge, this is the first implementation of a purely polysilicon and silicon nanocrystalline oxide slot waveguide platform.

©2013 Optical Society of America

OCIS codes: (130.3120) Integrated optics devices; (050.2770) Gratings.

---

## References and links

1. Q. Xu, V. R. Almeida, R. R. Panepucci, and M. Lipson, "Experimental demonstration of guiding and confining light in nanometer-size low-refractive-index material," *Opt. Lett.* **29**(14), 1626–1628 (2004).
2. R. Guider, N. Daldosso, A. Pitanti, E. Jordana, J. M. Fedeli, and L. Pavesi, "NanoSi low loss horizontal slot waveguides coupled to high Q ring resonators," *Opt. Express* **17**(23), 20762–20770 (2009).
3. K. Preston and M. Lipson, "Slot waveguides with polycrystalline silicon for electrical injection," *Opt. Express* **17**(3), 1527–1534 (2009).
4. T. Baehr-Jones, M. Hochberg, C. Walker, and A. Scherer, "High-Q optical resonators in silicon-on-insulator-based slot waveguides," *Appl. Phys. Lett.* **86**(8), 081101 (2005).
5. R. Sun, P. Dong, N. Feng, C.-Hong, J. Michel, M. Lipson, and L. Kimerling, "Horizontal single and multiple slot waveguides: optical transmission at  $\lambda = 1550$  nm," *Opt. Express* **15**(26), 17967 (2007).
6. A. Martínez, J. Blasco, P. Sanchis, J. V. Galán, J. García-Rupérez, E. Jordana, P. Gautier, Y. Lebour, S. Hernández, R. Guider, N. Daldosso, B. Garrido, J. M. Fedeli, L. Pavesi, J. Martí, and R. Spano, "Ultrafast All-Optical Switching in a Silicon-Nanocrystal-Based Silicon Slot Waveguide at Telecom Wavelengths," *Nano Lett.* **10**(4), 1506–1511 (2010).
7. R. Spano, N. Daldosso, M. Cazzanelli, L. Ferraioli, L. Tartara, J. Yu, V. Degiorgio, E. Giordana, J. M. Fedeli, and L. Pavesi, "Bound electronic and free carrier nonlinearities in Silicon nanocrystals at 1550nm," *Opt. Express* **17**(5), 3941–3950 (2009).
8. J. Shainline and J. Xu, "Silicon as an emissive optical medium," *Laser Photon. Rev.* **1**(4), 334–348 (2007).
9. J. V. Galan, P. Sanchis, J. Blasco, A. Martinez, and J. Martí, "High efficiency fiber coupling to silicon sandwiched slot waveguides," *Opt. Commun.* **281**(20), 5173–5176 (2008).
10. G. Roelkens, D. Vermeulen, S. Selvaraja, R. Halir, W. Bogaerts, and D. Van Thourhout, "Grating-Based Optical Fiber Interfaces for Silicon-on-Insulator Photonic Integrated Circuits" *IEEE J Sel. Top. Quantum Electron.* **17**(3), 571–580 (2011).
11. D. Taillaert, P. Bienstman, and R. Baets, "Compact efficient broadband grating coupler for silicon-on-insulator waveguides," *Opt. Lett.* **29**(23), 2749–2751 (2004).
12. M. Taillaert, K. B. Gylfason, and H. Sohlström, "An apodized SOI waveguide-to-fiber surface grating coupler for single lithography silicon photonics," *Opt. Express* **19**(4), 3592–3598 (2011).
13. D. Aiillaerta, F. Van Laere, M. Yre, W. Bogaerts, D. Van Thourhout, P. Bienstman, and R. Baets, "Grating Couplers for Coupling between Optical Fibers and Nanophotonic Waveguides" *Jap. J. Appl. Phys.* **45**(8A), 6071–6077 (2006).
14. G. Roelkens, D. Vermeulen, D. VanThourhout, R. Baets, S. Brision, P. Lyan, P. Gautier, and J.-M. Fédéli, "High Efficiency Diffractive Grating Couplers for Interfacing a Single Mode Optical Fiber with a Nanophotonic Silicon-on-Insulator Waveguide Circuit," *Appl. Phys. Lett.* **92**(13), 131101 (2008).
15. C. Xiong, W. H. P. Pernice, M. Li, and H. X. Tang, "High performance nanophotonic circuits based on partially buried horizontal slot waveguides," *Opt. Express* **18**(20), 20690–20698 (2010).
16. J. V. Galan, P. Sanchis, J. Blasco, and J. Martí, "Study of High Efficiency Grating Couplers for Silicon-Based Horizontal Slot Waveguides," *IEEE Photon. Technol. Lett.* **20**(12), 985–987 (2008).

17. N. N. Feng, J. Michel, and L. C. Kimerling, "Optical Field Concentration in Low-Index Waveguides," *IEEE J. Quantum Electron.* **42**(9), 883–888 (2006).
18. B. Wang, J. Jiang, and G. Nordin, "Compact slanted grating couplers," *Opt. Express* **12**(15), 3313–3326 (2004).
19. D. Taillaert, W. Bogaerts, P. Bienstman, T. F. Krauss, P. Van Daele, I. Moerman, S. Verstuyft, K. De Mesel, and R. Baets, "An Out-of-Plane Grating Coupler for Efficient Butt-Coupling Between Compact Planar Waveguides and Single-Mode Fibers," *IEEE J. Quantum Electron.* **38**(7), 949–955 (2002).
20. G. Roelkens, D. Van Thourhout, and R. Baets, "High efficiency grating coupler between silicon-on-insulator waveguides and perfectly vertical optical fibers," *Opt. Lett.* **32**(11), 1495–1497 (2007).
21. H. Yamada, M. Nozawa, M. Kinoshita, and K. Ohashi, "Vertical-coupling optical interface for on-chip optical interconnection," *Opt. Express* **19**(2), 698–703 (2011).
22. G. Roelkens, D. Van Thourhout, and R. Baets, "High efficiency Silicon-on-Insulator grating coupler based on a poly-Silicon overlay," *Opt. Express* **14**(24), 11622–11630 (2006).
23. D. Goldberg, *Genetic Algorithms in Search, Optimization, and Machine Learning* (Addison-Wesley, 1989).
24. Y. Tang, Z. Wang, L. Wosinski, U. Westergren, and S. He, "Highly Efficient Nonuniform Grating Coupler for Silicon-on-Insulator Nanophotonic Circuits," *Opt. Lett.* **35**(8), 1290–1292 (2010).
25. D. Kwong, J. Covey, A. Hosseini, Y. Zhang, X. Xu, and R. T. Chen, "Ultralow-loss polycrystalline silicon waveguides and high uniformity 1x12 MMI fanout for 3D photonic integration," *Opt. Express* **20**(19), 21722–21728 (2012).
26. P. Bienstman and R. Baets, "Optical modelling of photonic crystals and VCSELs using eigenmode expansion and perfectly matched layers," *Opt. Quantum Electron.* **33**(4/5), 327–341 (2001).
27. J. Ctyroky, S. Helfert, R. Pregla, P. Bienstman, R. Baets, R. De Ridder, R. Stoffler, G. Klaasse, J. Petracek, P. Lalanne, J.-P. Hugonin, and R. M. De La Rue, "Bragg waveguide grating as a 1D photonic band gap structure: COST 268 modelling task," *Opt. Quantum Electron.* **34**(5-6), 455–470 (2002).
28. T. Suhara and H. Nishihara, "Integrated Optics Components and Devices Using Periodic Structures," *IEEE J. Quantum Electron.* **22**(6), 845–867 (1986).
29. R. Emmons and D. Hall, "Buried-Oxide Silicon-on-Insulator Structures" *IEEE J. Quantum Electron.* **28**(1), 164 (1992).
30. S. K. Selvaraja, D. Vermeulen, M. Schaekers, E. Slecckx, W. Bogaerts, G. Roelkens, P. Dumon, D. Van Thourhout, and R. Baets, "Highly efficient grating coupler between optical fiber and silicon photonic circuit" presented at Lasers and Electro-Optics/International Quantum Electronics Conference, Munich, Germany (2009).
31. J. Goodman, *Introduction to Fourier Optics* (McGraw Hill, 1996), Chap. 9.
32. A. Martinez, S. Hernandez, P. Pellegrino, O. Jambois, P. Miska, M. Grun, H. Rinnert, M. Vergnat, V. Izquierdo-Roca, J. M. Fedeli, and B. Garrido, "Comparative study of the nonlinear optical properties of Si nanocrystals fabricated by e-beam evaporation, PECVD or LPCVD," *Phys. Status Solidi. C* **8**(3), 969–973 (2011).
33. K. Koukos, E. B. Edel-Pereira, O. G. Authier-Lafaye, E. Scheid, L. Bouscayrol, B. F. Ranc, P. Arguel, S. Bonnefont, F. Lozes-Dupuy, and G. Sarrabayrous, "Effect of Annealing Conditions on Photoluminescence Properties of Low-Pressure Chemical Vapour Deposition-Grown Silicon Nanocrystals" *Jap. J. Appl. Phys.* **47**(1), 130–132 (2008).
34. Q. Fang, J. F. Song, S. H. Tao, M. B. Yu, G. Q. Lo, and D. L. Kwong, "Low Loss (~6.45dB/cm) Sub-Micron Polycrystalline Silicon Waveguide Integrated with Efficient SiON Waveguide Coupler," *Opt. Express* **16**(9), 6425 (2008).
35. L. Liao, D. Lim, A. Agarwal, X. Duan, K. Lee, and L. Kimerling, "Optical Transmission Losses in Polycrystalline Silicon Strip Waveguides: Effects of Waveguide Dimensions, Thermal Treatment, Hydrogen Passivation, and Wavelength" *J. Electron. Mater.* **29**(12), 1380 (2000).
36. E. Ibok and S. Garg, "A Characterization of the Effect of Deposition Temperature on Polysilicon Properties," *J. Electrochem. Soc.* **140**(10), 2927–2937 (1993).
37. C. W. Holzwarth, T. Barwicz, and H. I. Smith, "Optimization of hydrogen silsesquioxane for photonic applications," *J. Vac. Sci. Technol. B* **25**(6), 2658–2661 (2007).
38. L. W. Luo, G. S. Wiederhecker, J. Cardenas, C. Poitras, and M. Lipson, "High quality factor etchless silicon photonic ring resonators," *Opt. Express* **19**(7), 6284–6289 (2011).
39. P. Pellegrino, B. Garrido, C. Garcia, J. Arbiol, J. R. Morante, M. Melchiorri, N. Dalbosso, L. Pavesi, E. Schied, and G. Sarrabayrouse, "Low-loss rib waveguides containing Si nanocrystals embedded in SiO<sub>2</sub>," *J. Appl. Phys.* **97**(7), 074312 (2005).

## 1. Introduction

Slot waveguides have become a platform of interest for integrated optics due to their ability to confine a guided mode into areas smaller than the diffraction limit [1]. However, due to the extreme confinement of light within the waveguide slots, scattering losses from such waveguides are extremely sensitive to thickness variations and/or roughness along an interface. Because of this sensitivity, horizontal slot waveguides, where the light is confined parallel to the substrate, are strongly preferred to vertical slots, as deposition, oxidation, and/or epitaxial growth can all routinely achieve near atomic flatness even for films only a few nanometers thick. This advantage yields superior propagation losses for amorphous and

polycrystalline silicon (polysilicon) horizontal slot waveguides (3 & 7 dB/cm, respectively) [2, 3] compared to vertical slot waveguides of single-crystal silicon (11.6 dB/cm) [4].

While crystalline/amorphous silicon slot waveguides have demonstrated lower propagation loss than their polysilicon counterpart, having a robust polysilicon slot platform is advantageous for three reasons. First, multiple slot configurations are obtainable with multiple deposited silicon layers, which can further confine light to narrower slot regions [5]. Second, the additional polysilicon layers can be doped and made electrically active, allowing for tunable and switchable electro-optic devices [3]. Third, unlike hydrogen-passivated amorphous silicon layers, polysilicon withstands a very high thermal budget, allowing for far greater process flexibility. For example, silicon nanocrystal oxide is commonly utilized as a slot material for its high nonlinear optical coefficients when annealed at high temperatures [6, 7]. Thus, further enabling a polysilicon, multi nanocrystal slotted platform for ongoing all-optical and electro-optical device characterization efforts is a necessity.

Despite silicon nanocrystals being lauded as a possible monolithic, on-chip laser source [8], sufficient lasing output has yet to be reported for any silicon medium, and consequently, external fiber-coupled light remains the dominant form of enlightening any silicon platform. Although inverse-tapered coupling structures have been proposed for horizontal slot waveguide fiber coupling [9], lensed fibers and small translation errors are required. In comparison, grating couplers are becoming an increasingly preferred solution for both the silicon-on-insulator platform [10–14] as well as for horizontal slot waveguides [15, 16]. Properly designed gratings may couple to standard single mode fiber with high efficiency and fiber translation tolerance without any need for cleaving, dicing, or polishing, allowing for timely in-line wafer testing.

Nevertheless, three issues remain which potentially impede the mass-manufacturability of horizontal slot grating couplers. First, obtaining acceptable coupling efficiencies without adding precise grating overlay deposition and lithography steps [10] is desirable from a manufacturing perspective. Second, achieving successful coupling to waveguides having more than one slot is desirable, as slot power confinement increases by 40% with a dual-slot waveguide and by 60% with a three slot waveguide [17]. Third, nearly all grating couplers demonstrated to date require angular detuning of the input/output fibers by a significant angle from normal incidence (~8-12 degrees) in order to eliminate significant back reflection and transmission problems [13] that will be derived in section 3. High throughput testing and mounting of fibers and/or vertical-cavity-surface-emitting-lasers (VCSELs) that are perfectly normal to the substrate would drastically increase device packaging reliability while also reducing packaging complexity and cost. Furthermore, while grating couplers must emit at the proper azimuthal angle to couple to an angularly detuned fiber, this is not the case for normally incident, unpolarized fibers. Using non-tilted fibers significantly relaxes waveguide routing constraints near vertically emitting grating couplers.

Although surface normal grating couplers exhibit potential advantages over angularly detuned gratings, previous surface normal couplers on silicon waveguides have required extreme fabrication complexity [18], an extensive bottom reflector [19], extra high resolution fabrication steps [20], or significant expansion of the device's footprint by simultaneously coupling to two counter-propagating waveguides [21]. Such elaborate workarounds are due to grating couplers often being designed solely from first principles with a single period and fill factor, effectively eliminating two of the most significant degrees of freedom available to a designer. To circumvent the difficulty of relaxing first-principle design, previous works have employed a genetic algorithm to slightly vary a traditionally designed grating in order to obtain marginal efficiency increases [18, 20, 22]. However, entirely departing from an initial first-principle design could manifest new structures that enable high performance coupling across many platforms, specifications, and fabrication constraints.

In this work, partially-etched, dual horizontal nanocrystal slot input/output grating coupler pairs were evolved via a genetic algorithm [23] (which is introduced in the following section) with no initial design, fabricated, re-evolved to match fabrication errors, and simultaneously coupled to and from a single mode fiber array at perfectly normal incidence.

## 2. Design methodology—genetic algorithm

In order to efficiently and maximally explore the potential design space for a fiber-grating coupler, the etch depth, deposited film thickness, period, and fill factor of each individual grating tooth must be considered. While variable etch depth for each grating tooth is a possible approach in grating design [24], preliminary 2D FDTD results over all feasible film thicknesses indicated that coupling efficiencies for two, three, and four slot gratings were not sensitive to etch depth as long as all slot layers were completely through-etched, as those layers contain the majority of guided light. In order to simplify fabrication without compromising coupling efficiency, all designs left the bottom silicon layer of the slot waveguide unetched, while all other waveguide layers were through-etched. This partially-etched profile yields higher emission toward the fiber and less emission toward the substrate through constructive and destructive vertical interference, respectively. Upward constructive interference was also maximized in 2D FDTD by fixing the buried oxide thickness to 2.38  $\mu\text{m}$ . The number and thickness of waveguide layers were optimized in RSoft FemSIM to maximize slot field confinement in a single mode horizontal dual-slot waveguide, as shown in Fig. 1. After this optimization, the top and bottom polysilicon layers are 128 nm thick, the middle polysilicon layer is 33 nm thick, and the two silicon nanocrystalline oxide slots are 27 nm thick. Although field confinement and grating coupling efficiency were shown in simulations to be higher in three or four slot waveguides, two slots were ultimately chosen to reduce fabrication complexity and increase yield in our research-grade fabrication facility.

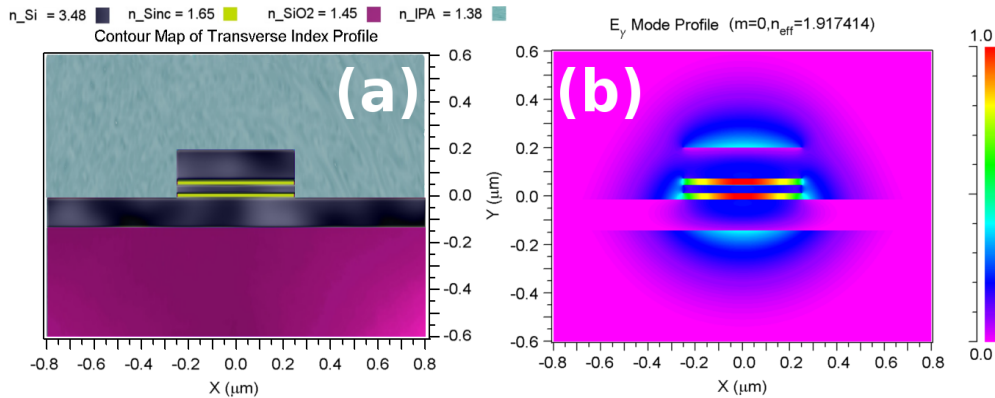


Fig. 1. (a) Rib-waveguide index profile obtained via partial etch. To simplify testing, isopropyl alcohol is the top cladding. The ripples in the polysilicon layers represent grain boundaries of approximate scale [25]. (b) TM mode profile of the multi-slot rib-waveguide, showing acceptable power confinement in the slots.

The two remaining design parameters for grating couplers are the period and fill factor. To maximally explore a grating's entire design space, individual grating teeth must be allowed different periods and fill factors. Because these parameters are no longer uniform for each grating tooth, the number of possible grating designs to consider increases geometrically. In order to find an optimum coupling efficiency despite this vast increase in design space, an in-house genetic algorithm was created from scratch where “genes” represent the period and fill factor of each grating tooth. Thus, the genetic code for a single grating design can consist of a number array of grating periods and fill factors. By programmatically converting this number array into a grating and inserting the structure into a photonic simulator capable of determining its fiber coupling efficiency, the “fitness” (coupling efficiency) of a particular “genetic code” (grating design) can be determined. After the efficiencies of many initial grating designs are obtained, the best designs within the group are selected to “mate” with each other in order to produce “children” grating designs. In the “mating” process, part of the number array of one grating design overwrites part of the number array of another grating design. In genetics, this process is known as “crossing over,” and the resulting design retains

characteristics from both parent designs. The newly created grating design then experiences “mutation,” where a single number of its genetic code is randomly selected and randomly altered. This final step may also be considered a simulated-annealing or a Monte-Carlo-like step to sufficiently perturb designs to ensure the algorithm does not settle on local optima within the design space. After the new designs are created, the algorithm may repeat itself by evaluating the new designs and selecting those with the highest coupling efficiencies for subsequent iterations. Although the above approach can eventually reach the global optimum of a design space, a very large number of grating simulations are usually required to obtain it, as each genetic generation produces tens of new designs to evaluate, and thousands to tens of thousands of design generations may be necessary. A flow chart of the entire iterative genetic evolution process is shown in Fig. 2.

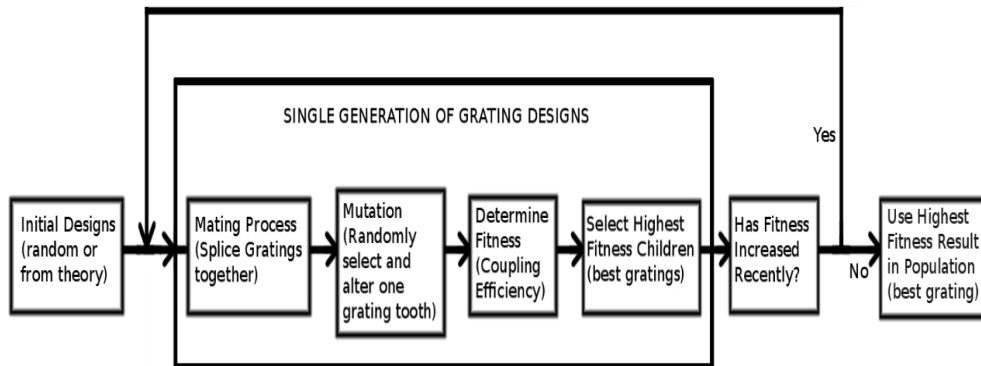


Fig. 2. Flow diagram of the iterative design process involved in evolving grating designs via a genetic algorithm.

For this particular design methodology to succeed over a realistic time interval, a single fiber-grating coupling efficiency must be simulated in tens of seconds or less. Because fiber-grating couplers usually contain strong index perturbations on scales near the wavelength of light, FDTD is most commonly used to simulate these structures. However, FDTD requires at least tens of minutes to complete a single grating simulation, which readily explains why grating couplers are typically designed solely from first principles, where uniform scattering and perfect phase-matching from an infinite number of periods are assumed in order to make the situation mathematically tractable (This approach is presented in the next section). This limitation leaves designers with far fewer degrees of freedom than are physically possible. Fortunately, a fully vectorial eigenmode expansion and propagation tool, known as CAMFR, has been developed that is capable of simulating grating couplers with arbitrary cross-sections and strong index contrast in tens of seconds or less [26, 27]. By successfully integrating the custom-made genetic algorithm with CAMFR, the resulting grating design suite is capable of exploring a very large possibility space for a particular photonic platform in weeks to months instead of years to decades. A single, standard desktop operating at 4 GHz was able to complete all computational work for this report within one month.

### 3. First-principle grating design

Although a genetic algorithm can explore large design spaces, its search efficiency is highly sensitive to initial design conditions. As with previous works, it was postulated that starting with designs created from first principles would take the fewest genetic iterations in achieving a global optimum [18, 20, 22]. A natural starting point is with the 2D Bragg condition which enforces longitudinal phase-matching between incoming and outgoing 2D plane waves due to an infinitely long 1D periodic disturbance [28, 29]:

$$\frac{2\pi n_{\text{eff\_out}}}{\lambda} \cos(\theta_{\text{out}}) = \frac{2\pi n_{\text{eff\_in}}}{\lambda} \cos(\theta_{\text{in}}) + \frac{q2\pi}{\Lambda} \quad (1)$$

Here,  $n_{\text{eff\_out}}$  is the effective index encountered by the outbound wave,  $\theta_{\text{out}}$  is the angle of the output light (where  $\theta = 0$  represents propagation along the waveguide),  $n_{\text{eff\_in}}$  is the effective index experienced by the incoming light,  $\theta_{\text{in}}$  is the angle of the input light,  $\lambda$  is the freespace wavelength,  $\Lambda$  is the grating period, and  $q$  is an integer of any value that denotes the grating's diffracted order. For the sake of discussion, the waveguide is considered the grating input, and the output is the emitted light directed towards the fiber. Care must be taken in choosing the proper  $n_{\text{eff\_in}}$ , as the majority of the input light will experience a number of grating periods that alter the input field into a quasi-Bloch mode before scattering to the output field [13].

Since this analysis serves as a starting design,  $n_{\text{eff\_in}}$  is chosen as 2.03, the effective index of the 12  $\mu\text{m}$  wide dual-slot waveguide abutting the 12  $\mu\text{m}$  wide grating. The input light moves along the waveguide, so  $\theta_{\text{in}} = 0$ , and since perfectly vertical fiber coupling is desired,  $\theta_{\text{out}} = \pi/2$ .  $q$  is set to  $-1$  because the majority of the input light must be redirected upward into a single diffraction order.  $\lambda = 1550$  nm, a ubiquitous optical telecommunications wavelength. This simplifies Eq. (1) to  $\Lambda = \lambda / n_{\text{eff\_in}}$ , which yields a grating period of 760 nm.

A more in-depth study of Eq. (1) reveals the underlying challenges to perfectly normal coupling.  $\theta_{\text{out}} = -\pi/2$  is also a solution to the above parameters, indicating that downward emission toward the substrate will occur. Furthermore,  $\theta_{\text{out}} = \pi$  if  $q = -2$ , meaning light may also be reflected back into the waveguide. If the equation is reversed so that the fiber is the input, then  $\theta_{\text{out}} = 0$  or  $\pi$ , meaning half of the coupled light will travel in the wrong direction away from the collecting waveguide. Coupling waveguides to either side of a vertically coupled grating circumvents this problem, but the coupler footprint is more than doubled, as two tapering and bending regions are needed to re-combine the bifurcated input [21]. In order to more elegantly break these symmetries and direct light solely to/from the fiber/waveguide, both a side distributed Bragg reflector (DBR) and reflection from the substrate should be employed [10, 30].

Finally, the Bragg condition above assumes an infinitely long grating, which is hardly the case, as high index contrast gratings are capable of radiating 100% of the input light in only a few periods. In order to see the effect of a finitely long grating, Fourier analysis of the grating profile is necessary [31]. First, the grating profile as a function of distance is:

$$g(x) = \left( \text{comb}\left(\frac{x}{\Lambda}\right) * \text{rect}\left(\frac{x}{\text{Aff}}\right) \right) \text{rect}\left(\frac{x}{L}\right), \quad (2)$$

where  $\Lambda$  is the grating period,  $\text{ff}$  is the grating fill factor (tooth width / period),  $L$  is the total length of the grating, and  $*$  denotes a convolution. The Fourier transform of Eq. (2) illustrates the grating's behavior in frequency space:

$$G(k_x) = \left( \text{comb}\left(\Lambda \frac{k_x}{2\pi}\right) \text{sinc}\left(\text{Aff} \frac{k_x}{2\pi}\right) \right) * \text{sinc}\left(L \frac{k_x}{2\pi}\right), \quad (3)$$

where  $k_x = 2\pi n_{\text{eff}} / \lambda$ . Three facts can be gleaned from this equation. First, diffraction orders arise when  $k_x = q2\pi / \Lambda$ . Second, the first diffraction order's emission strength is inversely proportional to the fill factor, while higher order efficiencies do not exhibit the same monotonicity. Third, each diffraction order has a frequency width inversely proportional to the total length of the grating.

The above analysis has proven useful by revealing four salient points. First, there are challenges in emission and reflection symmetries that must be overcome to achieve efficient normal coupling. Second, smaller fill factors yield higher diffraction efficiency while near unity fill factors hardly radiate at all. Third, shorter gratings exhibit wider bandwidths.

Fourth, an initial grating period of 760 nm was calculated for near-vertical emission and became the initial design for the genetic algorithm.

#### 4. Simulation and resulting structure

By using the first-principle design stated above, a grating with 15 periods of 760 nm followed by 30 periods of 380 nm, all with 50% fill factor, was fed into the genetic algorithm, where the shorter period created a side reflecting DBR. Despite the design having a DBR to redirect non-emitted light and a buried oxide of proper thickness to reflect downward emitted light, the initial fiber coupling efficiency was 27%. After only 300 generations, the genetic algorithm plateaued at 40% efficiency. The design's initial period was then swept from 710 nm to 810 nm and fed into the genetic algorithm, all of which resulted in the same 40% efficient grating design. The only significant alteration accomplished by the genetic algorithm was to introduce apodization (where the fill factor is ramped) in order to more smoothly transition the incoming light into the grating's Bloch mode and reduce back reflections into the waveguide [12]. The algorithm also introduced slight randomization into the DBR section, the effect of which will be explored further in the final design.

This settling of various first-principle designs into the same local optima indicated that drastically different initial conditions were required to obtain a global optimum in the design space. To this end, designs with purely random periods and fill factors for each grating tooth were then fed into the genetic algorithm. After a few hundred generations, a large number of grating designs had already surpassed the 27% efficiency obtained by the original first-principle design. After 10,000 generations, the genetic algorithm plateaued with a 68% grating-to-fiber coupling efficiency. Although CAMFR only simulated the structure's waveguide-to-fiber coupling efficiency, 2D FDTD also yielded the same efficiency for fiber-to-waveguide coupling, as was expected via the reciprocity condition. The resulting structure and its emission profile are shown in Fig. 3.

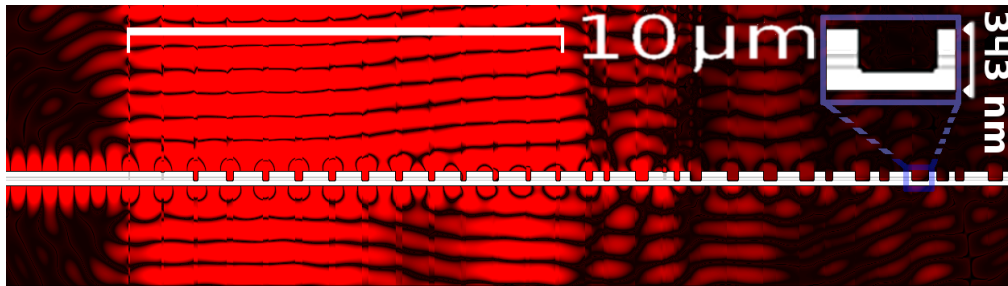


Fig. 3. Grating cross section showing simulated surface normal E-field emission to a fiber aperture from a waveguide on the left. Polysilicon is shown in white, and the silicon nanocrystalline oxide slots are in grey. The blue inset shows an enlarged view of a grating tooth. The etch depth for all sections is 215 nm.

In this final result, the genetic algorithm evolved a grating with four operational stages. In the beginning stage, the grating is apodized from a 95% to 82% fill factor in the first four teeth, which reduces the grating's initial emission strength, as was shown in Eq. (3) [10, 24]. By dampening the first stage's emission, the grating's field profile more closely matches the Gaussian mode of the vertically oriented fiber. In the second stage, the fill factor and period remain uniform for eight periods at 81% and 795 nm, respectively, and this stage is responsible for 70% of the grating's power coupling into the fiber. In the third stage, the period is chirped over six periods from 770 nm to 700 nm, and the fill factor becomes 86%. The chirp causes the third stage to emit light at a slightly negative angle of three degrees, which allows for an extra grating period to emit light into the fiber. Without this negative angle, the third stage's emission would not fit into the fiber's 10.4  $\mu\text{m}$  mode field diameter. Although a three degree emission will guide into the acceptance cone of a vertically oriented fiber, this creates a focal plane above the grating and slightly reduces the vertical translation

tolerance of the coupled fiber, which will be discussed later. The grating's final stage consists of a quasi-periodic DBR that reflects only 50% of light back into previous grating stages. When this stage is replaced by a uniform DBR with 99% reflectivity, the grating's overall coupling efficiency drops from 68% to 62%. This counter-intuitive result occurs because the beginning of the quasi-periodic DBR does not strongly reflect and instead emits a unique phase-front with side-lobes. When this emission is interfered with the emission from stage three, the resulting phase-front is flatter, narrower, and more Gaussian-like due to destructive interference, all of which increase the fiber coupling efficiency.

## 5. Fabrication and redesign

Starting with bare silicon wafers, the buried oxide layer was grown by wet thermal oxidation at 1050°C. First, purely amorphous silicon was deposited by low-pressure-chemical-vapor-deposition (LPCVD) of silane gas at 550°C, 260 mtorr, and 150 sccm. Next, a silicon-rich oxide layer was deposited by LPCVD of N<sub>2</sub>O and silane gases at 600°C, 270 mtorr, 40 sccm of silane, and 160 sccm of N<sub>2</sub>O. This specific method of depositing silicon nanocrystal can result in the highest obtainable Kerr coefficient and allows for superior thickness precision over plasma-enhanced-chemical-vapor-deposition (PECVD) [6, 32, 33]. Both depositions were repeated once more, followed by a final amorphous silicon deposition that completed all necessary layers for the horizontal dual-slot waveguide. Amorphous silicon is known to be highly absorbing at 1550 nm and must be properly annealed into long-grain polysilicon in order to reduce its absorption loss [25, 34, 35]. Furthermore, silicon nanocrystals in the oxide slots must precipitate to only 1 to 4 nm in diameter to exhibit a large Kerr nonlinearity, which is accomplished in a high temperature anneal step [33]. Prior to annealing, the wafers were set in atmosphere for a week to allow a native oxide to form, which prevents strain relaxation, buckling, and high surface roughness from occurring in the top silicon layer during annealing, to which TM polarized waveguides, such as horizontal slots, are extremely sensitive [36]. Next, the wafers were annealed in N<sub>2</sub> gas at 600°C for 10 hours. Ellipsometry confirmed a drop in the index of refraction of all silicon layers from 3.58 to 3.48, indicating the silicon's amorphous structure had evolved into a polycrystalline structure. However, the silicon layers were thinner than the polysilicon grain sizes achievable by a low-temperature anneal step (200-300 nm). Such short-grain polysilicon layers require a high temperature anneal step to ensure maximum crystallinity and minimum light absorption in the silicon layers. In order to fully crystallize the polysilicon layers as well as precipitate silicon nanocrystals out of the silicon-rich oxide slots, the wafers were then subjected to one second of 1100°C rapid thermal annealing. Finally, in order to fit the samples into subsequent processing steps, the wafers were cleaved into 2x2 cm chips using a diamond-tipped scribe and glass pliers. Final ellipsometry of the chips confirmed that silicon crystallization and nanocrystal precipitation had occurred, as the silicon layers ended with an index of 3.47, and the oxide slot layers rose from 1.48 to 1.65. However, ellipsometry also revealed a +/- 5 nm error in the final thickness of all layers from their target thicknesses previously stated in section 2.

The fabricated layer thicknesses reduced the grating's simulated coupling efficiency to 50%. By inserting the true layer thicknesses into the genetic algorithm, minor modifications to the design re-obtained a 68% theoretical coupling efficiency after 2,000 additional generations. This new design was then patterned in ZEP-520A resist by a 50 kV JEOL 6000 electron beam system at 100 pA. The developed resist pattern was then etched with alternating reactive-ion-etching cycles of HBr + Cl<sub>2</sub> and CHF<sub>3</sub> + O<sub>2</sub> chemistry. SEM analysis of 20 etched grating patterns revealed a stochastic error of 3 +/- 20 nm of width and translation error for each grating line. Re-simulating the grating with this source of error lowered its theoretical efficiency to 55%. After programming this source of error into the genetic algorithm, a design plateau was reached after 5,000 generations with a new theoretical efficiency of 63% that proved highly resilient to stochastic variations of fill factor and/or position of each grating tooth. The latest fabrication-tolerant grating design was then patterned, exposed, and etched. A top-down SEM of the completed grating is shown in Fig. 4.

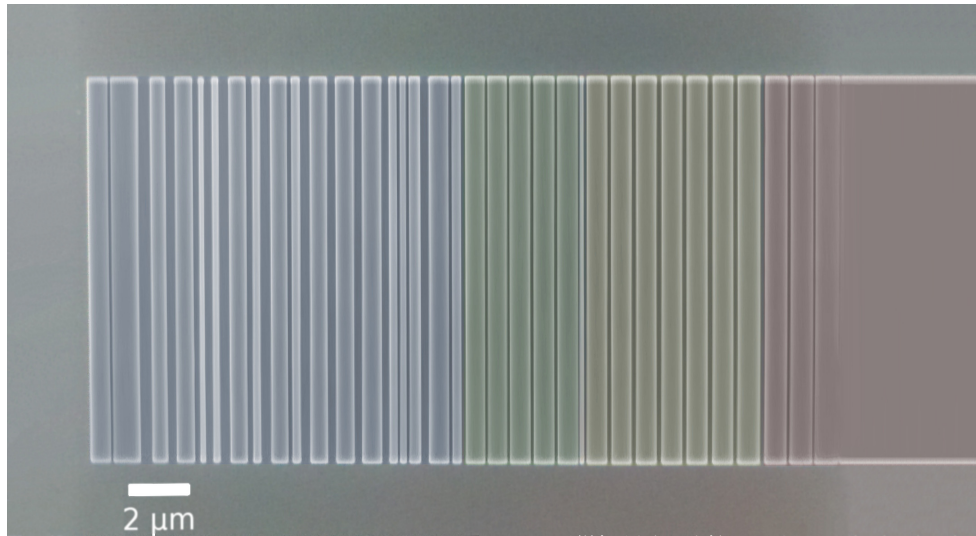


Fig. 4. Colorized SEM depicting each grating stage. Red is the apodized grating/waveguide interface, yellow is the primary fiber-coupling region, green is the secondary coupling region of chirped grating period, and blue is the quasi-periodic DBR to partially emit and reflect light back into previous grating stages.

## 6. Testing and results

In the chip layout, identical 12 μm wide input/output gratings were connected to 500 μm long waveguides that adiabatically tapered their widths from 12 μm to 500 nm. These single mode waveguides were then connected via a circular 125 μm radius u-turn, as shown in Fig. 5(a). In order to characterize the gratings' spectral coupling performance, broadband TM light must be coupled and measured, as the grating coupler is designed for a horizontal slot waveguide, which requires a vertically oriented E-field (TM) to confine light into the slots. If a horizontally oriented E-field (TE) is used, the polysilicon layers would instead guide the majority of the light. The grating would then consist of significantly different effective indices from its intended design, causing it to interfere the light from all four grating stages and emit a haphazard field profile with negligible fiber coupling efficiency.

Thus, amplified spontaneous emission spanning 1530 nm to 1610 nm and centered at 1558 nm from an erbium doped fiber array was passed through a TM polarizer and connected to a fiber array. The fiber array contained standard polarization maintaining, single mode fibers that were spaced 250 μm apart. Subsequently, the array was mounted to a 6-axis stage possessing 50 nm and 0.3 arcseconds of resolution. The 2x2 cm chip containing the fabricated gratings was mounted to a standard 3-axis stage, making the chip's surface parallel to the incoming fiber array facet. The experimental coupling setup and a schematic of the fiber-grating-waveguide coupling are shown in Fig. 5.

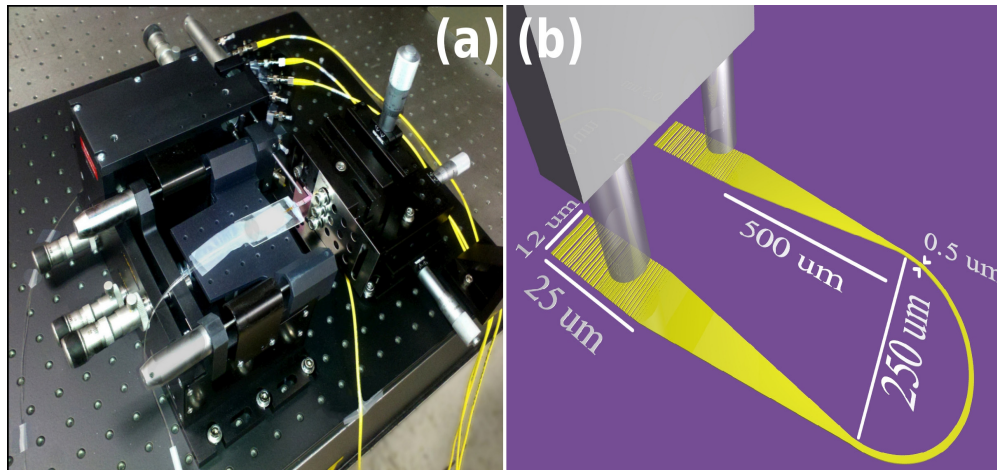


Fig. 5. (a) Experimental lab setup for perfectly normal coupling between a standard fiber array and on-chip gratings. (b) Illustrated chip layout coupled to a normally-incident input/output fiber array.

Spin-on-glass with an extremely low viscosity (0.6 cSt), high thermal budget, and proper superstrate index of refraction [37] as well as high quality  $\text{SiO}_2$  deposition were unavailable. Therefore, isopropyl alcohol (IPA), which also has an acceptable index of refraction near that of fiber (1.38) and a low viscosity (1.9 cSt) necessary for filling potentially narrow grating teeth lines, was chosen as the top cladding in order to simplify and expedite optical testing. After positioning the fiber array less than  $50 \mu\text{m}$  above the chip surface, IPA was dispensed onto the fiber array, which remained between the array and chip surface for several minutes due to sufficient surface tension and minimal evaporative surface area at such short distances. Next, the fibers within the array were aligned approximately  $2 \mu\text{m}$  above the grating couplers at perfectly normal incidence. The broadband signal was then passed through the input fiber, and an optical spectrum analyzer collected the output.

The setup's total loss was 43.4 dB. In order to extract the slot waveguide's propagation loss, a ring resonator was then patterned  $250 \text{ nm}$  adjacent to the single mode waveguide, and the device was re-measured. The ring's resulting parameters were a  $20 \mu\text{m}$  radius, a  $12.6 \text{ nm}$  free spectral range, a  $17.3 \text{ dB}$  extinction ratio, and a loaded Q factor of 535. These parameters allow for the propagation loss within the ring resonator to be calculated, resulting in a propagation loss of  $280 \text{ dB/cm}$  for the dual-slot single mode waveguide [38]. This extreme loss is a direct result of very high surface roughness ( $\sim 20 \text{ nm}$ ) of the oxide slots, as the oxide films did not reflow during annealing due to constraining film stress with the polysilicon layers. It is important to emphasize that in future work, each oxide layer must be annealed individually before a covering deposition is performed. Because the embedded silicon nanocrystals themselves do not exhibit large scattering losses, allowing the slot layers to properly reflow is expected to vastly improve this platform's propagation loss in future iterations [39]. After accounting for propagation loss, the remaining  $4.4 \text{ dB}$  of loss is allocated evenly between the input/output gratings.

After normalizing for the ASE source, the result is shown in Fig. 6, where a single grating of the input/output pair yielded a peak efficiency of 60.1% or  $-2.2 \text{ dB}$  at  $1555.8 \text{ nm}$ . The output power was maximized when the fiber array was exactly normal to the chip surface. The 3 dB in-plane coupling tolerance of the fiber array was approximately  $2 \mu\text{m}$  in both dimensions. As mentioned in section 4, the measured vertical coupling tolerance was lower than the Rayleigh range of the combined grating couplers, as the total coupled power was halved when the fiber array was approximately  $30 \mu\text{m}$  above the gratings. This result is likely due to the focusing effect introduced by the chirped grating stage as well as a non-Gaussian-like field arising from interfering all four grating stages at ever higher planes above the chip surface. The shift from the designed  $1550 \text{ nm}$  peak is due to the final design uniformly

overcompensating for the aforementioned lithography errors, leading to tooth width variance slightly exceeding trench variance during e-beam writing. This slightly increased fill factor increased the grating's propagation constant, weakened the grating, and shifted emission to longer wavelengths. The fiber array contains up to 0.5  $\mu\text{m}$  of translational misalignment between its fibers, which accounts for the 2.9% discrepancy between measured peak efficiency and theoretical expectation.

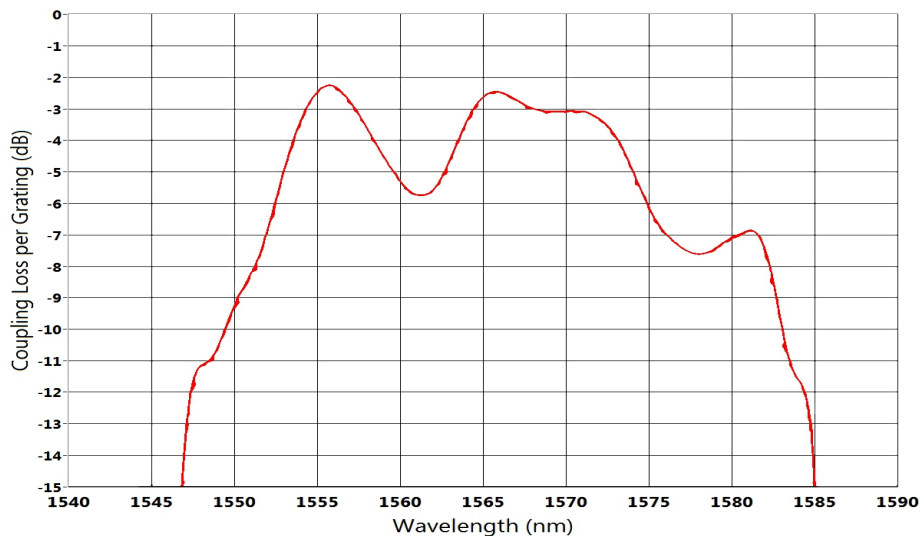


Fig. 6. Experimentally measured spectrum of single mode fiber coupling efficiency to/from a fabricated multiple horizontal slot grating. The data are normalized to the ASE source and for a single grating coupler.

## 7. Conclusion

Efficient grating coupling from a normally incident fiber array to multiple horizontal slot waveguides have been experimentally demonstrated with a 60.1% coupling efficiency per grating. Starting from purely random designs, simulations from a custom genetic algorithm created a four stage grating coupler with a theoretical efficiency of 68%. In contrast, a traditional coupler designed solely from first principles yielded a 27% theoretical efficiency and plateaued at 40% when augmented with the genetic algorithm. By then introducing measured fabrication errors into the genetic algorithm, a robust design with a 63% theoretical efficiency was derived from the 68% design. In the future, such an error incorporation scheme into a genetic algorithm may effectively and simultaneously design around many additional constraints and/or transients imposed in the real world. For example, while having large coupling bandwidth was not a design target in this work, future work may vary the operating wavelength during genetic iterations in order to pressure a design into accommodating an arbitrary frequency band. Other parameters may also be varied such as fiber translation, fiber rotation, fiber damage, grating damage, superstrate index variation, changing bandwidth requirements, or even grating performance tunability through refractive index modulation. This work demonstrates the potential benefit and flexibility afforded in novel silicon photonic platforms when efficient design-space searching algorithms are utilized in lieu of brittle first-principle design methodologies.

## Acknowledgments

Financial support from the Cullen Trust For Higher Education is gratefully acknowledged. Invaluable chip layout design support from the IPKISS project, Pieter Dumon, and Matthias Köfferlein are all emphatically acknowledged and appreciated.